Preparation of mesoporous batatas biochar via soft-template method for high efficiency removal of tetracycline

Zhihong Zheng[1,2], Baolong Zhao[1,3], Yiping Guo[1,3],

Yujie Guo[1,3], Tannaz Pak[4], Guoting Li[*,1,3]

1. *School of Environmental and Municipal Engineering, North China University of Water Resources and Electric Power, Zhengzhou 450046, China*
2. *Henan Vocational College of Water Conservancy and Environment, Zhengzhou 450008, China*
3. *Henan Key Laboratory of Water Environment Simulation and Treatment, North China University of Water Resources and Electric Power, Zhengzhou 450046, China*
4. *School of Computing, Engineering & Digital Technologies, Teesside University, Borough Road, Middlesbrough, TS1 3BX, UK*

***Corresponding author:** Tel: +86-371-69127538; Fax: +86-371-65790239;

E-mail: liguoting@ncwu.edu.cn (G.T. Li)

Abstract

In this contribution, we apply a soft-template-assisted hydrothermal route using polyethylene-polypropylene glycol (F127) as soft-template agent and biomass batatas

as carbon precursor to synthesis a novel hydrothermal mesoporous biochar (HMC-800) for adsorptive removal of tetracycline (TC) from wastewater. We use the biochar prepared without F127 and direct pyrolytic biochar for comparison. The physicochemical properties of all the studied biochar samples are measured using a suite of characterization techniques. Our results show that the HMC-800 displays the highest specific surface area (286.3 m^2/g) and total pore volume (0.249 cm^3/g), manifesting the introduction of F127 can result in formation of well-developed pore structures. Regarding adsorption properties, the HMC-800 outperforms other biochar samples for TC removal. Our finding shows that solution with near-neutral pH is favorable for TC removal, and the highest adsorption capacity is observed at initial solution pH value 7. In addition, our findings show that applying the pseudo-second-order kinetic and Freundlich isotherm equation closely models the recorded adsorption behavior. The maximum adsorption capacity is measured to be as much as 238.7 mg/g by Langmuir isotherm model. Pore filling, hydrogen-bonding and n-π interaction are suggested to be the prevailing adsorption mechanisms compared to the other mechanisms. Furthermore, the HMC-800 performs better in regeneration and reuse experiments, making it a promising adsorbent material for TC removal from wastewater.

Keywords: Adsorption, Batatas, Mesoporous biochar, Soft-template method, Tetracycline

1. Introduction

Tetracyclines (TC) are a common drug and personal care product which have been widely used to prevent bacterial infection in humans, flora, and fauna. TC are one of the most frequently used antibiotics worldwide (Cao et al., 2019; Tomul et al., 2020; Zandipak and Sobhanardakani, 2018). A main issue surrounding the use of TC at such large scale is that TC are difficult to degrade as they have a particularly stable structure caused by the existence of naphthol rings in their structure. When consumed by an organism only a small part of TC becomes inactive through hydroxylation, dissociation, glucoside acidification, and other metabolic reactions. This causes discharging of the vast majority of TC into the environment in their original forms or as metabolite by the fecaluria of patients, livestock, and poultry. This is known to cause soil and water contamination and potential continuing unfavorable threat to human health as well as the natural ecological systems (Delgado-Moreno et al., 2021; Yu et al., 2009). To deal with this problem a growing number of processes (chemical technologies such as adsorption or oxidation, biotechnologies, and physical technologies) are currently used for TC removal from wastewater (Huang et al., 2020; Xu et al., 2020). Comparatively speaking, adsorption is regarded as a favorable wastewater treatment technology owing to its low energy consumption, simple operation, high efficiency, and high resource availability (Ghoochian et al., 2018; Sobhanardakani and Zandipak, 2018; Ardakani et al., 2020).

In recent years, porous carbon materials are recognized as promising adsorbents

used to adsorb antibiotics from wastewater. Examples of porous carbon materials are activated carbon, magnetic ordered mesoporous carbon, graphene oxide, hierarchically porous carbon monoliths, and functionalized carbon nanotubes (Hu et al., 2019; Kueasook et al., 2020; Martins et al., 2015; Xiong et al., 2018; Yu et al., 2017). Porous carbon materials could be synthesized through traditional direct pyrolysis as well as hydrothermal pyrolysis methods. In using pyrolysis, more activation mediums (such as KOH, NaOH, and $ZnCl_2$) are required to obtain high porosity porous carbon material, as well as the addition of other metal oxides assists with improving the performance of the produced material (Zhang et al., 2020; Zhou et al., 2020). Introduction of chemical substances as activation agents result in the possibility of secondary pollution as the porous carbon materials are applied in adsorption process. As a solution, the template method has attracted significant attention. The carbon materials obtained using template method not only display plentiful oxygen-containing groups and large specific surface area, but also allow effectively control over the pore shapes, pore size distribution, pore arrangements, and material appearance (Li et al., 2020; Li et al., 2006; Wu et al., 2019; Xiao et al., 2017).

In general, according to properties of template, the template methods are classified into the two groups of hard-template and soft-template methods (Feng et al., 2014; Inagaki et al., 2016). The hard-template method requires use of corrosive acids or alkali chemical reagents to remove the template. This results in a complicated

treatment process, comparatively higher costs, and challenges in mass production. In contrast, soft-template method is preferable due to its simplicity of application and low-cost. (Kueasook et al., 2020; Wu et al., 2019). For example, Zhao and coworkers reported on successful synthesis of ordered mesoporous carbon materials with various arrangements and structures by changing the composition and concentration of the soft-template agent. In their study, PEO-PPO-PEO and phenol/formaldehyde were used as the soft-template agent and carbon source precursor, respectively (Meng et al., 2006). In another relevant study, Li and co-workers synthesized ordered mesoporous carbon material by using P123 and sucrose as their soft-template agent and carbon precursor, respectively (Li et al., 2006). Similarly, Zhao and co-workers synthesized well-aligned mesoporous carbon by using F127 and cyclodextrin as the soft-template agent and carbon source precursor, respectively (Feng et al., 2014). The prepared carbon materials are commonly used in batteries, supercapacitors, and electrocatalysts (Wu et al., 2018; Xiao et al., 2017). However, little attention has been paid to investigating the use of synthesized porous carbon materials (produced using soft-template method) in environment remediation.

It is known that the adsorption performance of an adsorbent is highly dependent on the number and distribution of adsorption sites. The above-mentioned soft template method can offer the expected pore structure, which may generate a significant number of adsorption sites. Therefore, porous carbon materials prepared using the soft-template method have an excellent adsorption prospect. Hu and co-workers

synthesized magnetic mesoporous carbon materials using F127 and phenolic resin as the soft-template agent and carbon source precursor for adsorption of minocycline. The maximum adsorption capacity was reported to be up to 224.3 mg/g at 25 ℃ (Hu et al., 2019). Kueasook and co-workers used F127 and phloroglucinol/glyoxylic acid as the soft-template agent and carbon source precursor, using sugarcane bagasse as scaffold, to synthesize a hierarchical porous carbon material. They reported with high adsorption efficiency for methylene blue (Kueasook et al., 2020). In application of soft-template method, organic polymers or biomass derivatives are commonly used as carbon source precursors during the preparation step, which increases the costs. Considering the renewable nature and the low cost of natural biomass, biomass derived mesoporous carbon materials shows great promise for large-scale production.

Biomass has rarely been used directly as a carbon source precursor to prepare delicate carbon materials by adding a soft-template agent. In this work, we report on synthesis of a novel hydrothermal mesoporous biochar through application of the soft-template method. We use biomass batatas and F127 as the carbon source precursor and the soft-template agent, respectively. During the synthesis process, the organic self-assembly function between organic template molecules F127 and the carbon precursor batatas occurs in hydrothermal carbonization process. Subsequently, the soft-template is removed through the pyrolysis process. We also prepare biochar samples without use of F127 and direct pyrolytic biochar for comparison. We present the comparison of the physical structures and chemical properties of these three

biochar samples using SEM-EDS, BET, FTIR, XRD, and Raman analysis. Moreover, the TC adsorption performance/mechanisms of HMC-800 are particularly studied through a series of adsorption experiments.

2. Materials and methods

2.1 Materials

Batatas as carbon precursor was obtained from local outdoor market in Zhengzhou City, China. Tetracycline (TC) and polyethylene-polypropylene glycol (F127, average Molecular Weight ~ 13000) were provided by the Macklin Co. (Shanghai, China). All chemicals were used without further purification in this study. Other chemicals were analytically pure and provided by Kermel Chemical Reagent (Tianjin, China), including sodium hydroxide, hydrochloric acid, sodium nitrate, sodium sulfate, sodium bicarbonate, and sodium phosphate.

2.2 Preparation of the mesoporous batatas biochar

Firstly, the obtained batatas was washed and oven-dried at 80 ℃. Then, a multi-function pulverizer was used to grind the dried raw batatas. The produced material was sieved through a 100-mesh screen. A 1.0 g sample of F127 was melted at 50 ℃ for 30 minutes in 20 mL of deionized (DI) water. Subsequently, 2.0 g of batatas powder was mixed with this sample and stirred for 30 minutes. After ultrasonication treatment at 100 HZ for 15 minutes, the mixture was transferred into a hydrothermal reactor and stored at 160 ℃ for 6 h. The obtained black solid product was rinsed with DI water several times, before it was dried at 80 ℃ overnight. Finally, the dried black

solid product was pyrolyzed in a tubular furnace from indoor temperature to 800 ℃ with a heating rate of 5 ℃/min and was stored under vacuum for 2 h (Wu et al., 2019). The resulting carbon powder was collected and labeled as HMC-800.The carbon prepared without F127 was named as HBC-800. The carbon prepared by direct pyrolysis at 800 ℃ was labeled as PBC-800.

2.3 Material characterization

The morphology and superficial element compositions of HMC-800, HBC-800, and PBC-800 were characterized using SEM and EDS (Hitachi S-8010). The textural properties of HBC-800, PBC-800, virgin and exhausted HMC-800 were evaluated on the basis of Brunauer-Emmett-Teller method (BET, ASAP2020). Surface functional groups were measured by Fourier transform infrared spectroscopy (FTIR, Thermo Fisher Nicolet iS5) and X-ray photoelectron spectroscopy (XPS, Thermo Scientific Escalab 250Xi). The structural configurations were studied by an X-ray diffractometer (XRD, X'Pert^3 Powder), and Raman spectrometer (Renishaw inVia reflex). The Zeta potential of HMC-800 was determined by a Malvern Zetasizer (Nano ZS90 analyzer) to obtain the point of zero charge (pH_{PZC}).

2.4 Adsorption experiments

The TC adsorption capacity on the prepared biochar samples was determined by the following batch experiments. A certain amount of biochar was dispersed in 50 mL TC solution (20 mg/L). The initial pH of the solution was adjusted by using 0.1 M NaOH or 0.1 M HCl. For the kinetic study, 200 mg of adsorbent was dispersed in a 1

L of 20 mg/L TC solution and stirred at a constant rate. At desired time intervals, the TC solution was collected and determined. For the adsorption isotherm study, the adsorption experiments were performed with different TC concentrations ranging from 10 to 400 mg/L. In order to achieve adsorption equilibrium, the above solution was shaken at 150 rpm for 24 h. All experiments were kept at 25 ℃ and at pH 7 unless otherwise stated. In addition, the concentration of TC containing before and after adsorption was measured by UVmini-1240 spectrophotometer (Shimadzu, Japan) at its maximum absorbance wavelength of 360 nm. The adsorption capacity and removal efficiency were estimated according to the equation (1) and (2):

$$q_e = \frac{V(C_0 - C_e)}{m} \quad (1)$$

$$R = \frac{C_0 - C_e}{C_0} \times 100\% \quad (2)$$

where q_e (mg/g) is the adsorption amount of TC at equilibrium; C_0 and C_e (mg/L) denote the TC concentration at initial and equilibrium moment, respectively; R represents the removal efficiency of TC; and V (L) and m (g) are the reaction solution volume and the weight of biochar samples, respectively.

2.5 Regeneration experiments

The exhausted biochar samples were collected, rinsed with DI water, and then stored at 80 ℃ overnight. NaOH (0.1 M), ethanol (mass fraction of 95%), and thermal treatment were used respectively for biochar regeneration. To achieve this, 100 mg sample of the exhausted biochar was added to 100 mL of the desorbing agent (NaOH or Ethanol) and shaken for 24 h, as well as thermally degraded at 800 ℃ over 2 h. The

regenerated biochar was used for adsorption experiments using 50 mL of TC solution (20 mg/L) and 10 mg of biochar at 25 ℃ and pH 7. The same regeneration and reuse experiment procedures were cycled 4 times.

3 Results and discussion

3.1 Characterization of the mesoporous batatas biochar

The morphology and structure of the prepared biochar samples are firstly characterized by SEM (Fig. S1). PBC-800 exhibits a flaky texture with a smooth and non-porous surface. In contrast, HMC-800 and HBC-800 display a variety of interconnected spherical particles with smooth surfaces, which is attributed to the degradation of amylum component during hydrothermal carbonization treatment and subsequent precipitation and growth processes (Simsir et al., 2017). A similar morphological observation was reported by a previous study (Jain et al., 2016). However, without F127 as soft-template agent, HBC-800 conglomerates into carbon blocks, with surfaces covered with carbon particles and irregular spheres. HMC-800 possesses interconnected and perfect carbon spheres with relatively uniform sizes. The above results demonstrate that the using of soft-template F127 plays a key role in the morphology and structure of the produced biochar. Meanwhile, the quantitative analysis of elemental composition by XPS (Table 1) and EDS (Fig S1) indicates that the three biochar samples studied here are typical carbon product judged from their high carbon contents (above 80%), which shows that they possess strong chemical stability and high mechanical strength (Tran et al., 2020).

A further study is performed using N_2 adsorption/desorption analysis (BET) to measure the pore structure and pore size distribution of the three biochar samples under studies. It is found that the N_2 isotherms of all carbon materials satisfy a type IV pattern with hysteresis loop (see Fig. S2a), which suggests that the numerous mesopores are existent in these samples (Huang et al., 2020; Li et al., 2020). The pore size distribution curves calculated from BJH model reveal smaller size mesopores and larger size mesopores formed the majority in HMC-800 and PBC-800 (Fig. S2b, c, and d), respectively. The average pore diameter is measured at 2.59 and 3.90 nm for two samples, respectively. The intense peaks of HBC-800 located at approximately 2~4 nm and 71.0 nm indicate that there are complex pore structures including both mesopores and macropores.

Moreover, the Table 1 shows the textural properties of the biochar samples, indicating that the HMC-800 has higher specific surface area of 286.3 m^2/g (22.0 and 15.9 times larger than that of HBC-800 and PBC-800, respectively) and total pore volumes of 0.249 cm^3/g (7.1 and 6.9 times larger than that of HBC-800 and PBC-800, respectively). The above results clearly illustrate that the soft-template method can improve the specific surface area and porosity of carbon materials. The proportion of mesopores in HMC-800, HBC-800 and PBC-800 was 79.4%, 89.4% and 94.9%, respectively. It is known that the length, width, and thickness of the TC molecule are 1.41, 0.46, and 0.81 nm, respectively. Literature studies show that an adsorbent displays the best adsorption performance when its pore sizes are 1.7~3 times higher

than the size of contaminant molecule (Zhang et al., 2019b). Considering the pore-size distribution of HMC-800, it is clear that HMC-800 has the correct range of pore-sizes for adsorption of TC molecules. This suggests that HMC-800 is a suitable option for TC adsorption.

Table 1

FTIR spectra is measured to investigate the surface chemistries of the synthesized biochar samples. The spectra obtained for HMC-800, HBC-800, and PBC-800 are similar, indicating that their surface functional groups are similar. As shown in Fig. 1(a), the band located at 3420-3450 cm^{-1} is assigned to the -OH group (such as phenol, carboxylic groups, and even absorbed water). The band at around 2915-2925 cm^{-1} is ascribed to the presence of -CH, $-CH_2$ and $-CH_3$ groups in aliphatic acids or alkanes. Further, the C=O bond conjugated carboxylic, and lactonic groups at approximately 1580-1595 cm^{-1}, especially that for HMC-800, and HBC-800, are clearly observed. The characteristic band at 1040-1200 cm^{-1} is originated from the stretching of C-O bond (ethers or lactones groups) (Delgado-Moreno et al., 2021; Sekulic et al., 2019). These oxygen-containing groups act as π-electron acceptors during the reaction, which can link with aromatic contaminants through hydrogen-bonding and n-π interaction (Sewu et al., 2019). Moreover, the band at around 1400-1425 cm^{-1}, representing C=C bond (aromatic rings), manifests the formation of relatively stable aromatic compounds. The C=C bond intensity on the HMC-800 and HBC-800 significantly strengthens compared to that for PBC-800,

suggesting more existing aromatic rings on the HMC-800 and HBC-800 than that on the PBC-800, which contribute to capturing the aromatic contaminants through π-π interactions (Tomul et al., 2020). This demonstrates that the applied hydrothermal process is favorable for formation of the surface functional groups involved in adsorption process as well.

To obtain detailed information of surface functionalities, C 1s photoelectrons analysis (Fig. S3 and Table S1) is detected. The C 1s peaks can be fitted to five curves. These peaks are attributed to aliphatic/aromatic carbon groups (C-C, C=C and C-H, 284.6-284.8 eV), hydroxyl groups (C-O-H, 285.1-285.4 eV), carbonyl groups (C=O, 286.5 eV), carboxylic/ester/lactone groups (O=C-O, 288.6 eV), and π-π^* band at around 290.8 eV due to the significant levels of π electrons from aromatic rings (Choi et al., 2020; Pereira et al., 2015; Wang et al., 2019). The chemical state distribution shows that the proportion of oxygen-containing functional groups of HMC-800 and HBC-800 (about 42.90% and 46.43%) is distinctly higher than that of PBC-800 (about 33.19%), this can be linked to the applied hydrothermal carbonization treatment.

Fig. 1

Raman spectroscopy is conducted to characterize the structural features and graphitization degree for the samples under study. Fig. 1(b) shows the two distinctive characteristic peaks of the Raman spectrum (D-band and G-band) at around 1340 and 1590 cm^{-1}, respectively. These peaks are linked with sp^3 hybrid configuration of C

representing disorder and defect structure and the sp^2 hybrid configuration of C representing crystalline graphite structure (Shang et al., 2019). Qualitatively, the intensity ratio of two peaks (I_D/I_G) reflects the defect degree of the carbon material. The values of I_D/I_G for our three biochar samples are all smaller than one, i.e. HMC-800 (I_D/I_G = 0.865) < HBC-800 (I_D/I_G = 0.872) < PBC-800 (I_D/I_G = 0.880). The results demonstrate that the prepared carbon materials have a less profound defect property and a higher degree of graphitization (Pachfule et al., 2016). We can, therefore, conclude that the presence of more aromatic C=C bonds could improve TC adsorption via π-π interaction. In addition, HMC-800 has a lower I_D/I_G value than HBC-800, which indicates that the application of F127 can improve the graphitization degree for these carbon materials. This finding is consistent with the observations previously reported in the literature (Wu et al., 2019).

The crystalline structure of biochar samples is analyzed by XRD technique (Fig S4). Results show that HMC-800 and HBC-800 display similar diffraction peaks. The bands located at around 2θ = 23.2° and 2θ = 43.3° are linked to the crystal planes (002) and graphitic planes (100), respectively. This finding indicates that HMC-800 and HBC-800 possess an amorphous carbon structure and a graphitic structure, which contributes to the π-π interaction with aromatic rings of TC. Furthermore, other observed diffraction peaks at around 2θ = 29.5°, 2θ = 36.1°, 2θ = 37.4°, and 2θ = 39.5° can suggest existence of miscellaneous inorganic components, such as whewellite and calcite minerals, in the raw material (Gong et al., 2019). However, only two weaker

diffraction bands are identified at around 2θ = 23.2° and 2θ = 43.3° in the XRD pattern detected for PBC-800. This indicates that the graphitization and crystallinity degree of PBC-800 are lower than HMC-800 and HBC-800. These weak peaks may have originated from the decomposition of whewellite and calcite during pyrolysis.

3.2 Adsorption performance

The adsorption performance of the three biochar samples studied here for TC is presented in Fig. 2(a). It demonstrates that HMC-800 has the highest adsorption capacity (55.0 mg/g), which is particularly higher than that of PBC-800 (3.3 mg/g) and HBC-800 (22.7 mg/g). It also evidences that the applied preparation procedure for HMC-800 using soft-template method is successful in achieving outstanding adsorption capability for TC. As such, HMC-800 is preferably used in the subsequent experiments.

3.2.1 Effect of adsorbent dose and initial TC concentration

Effect of adsorbent dose on the TC adsorption removal is shown in Fig. 2(b). The removal efficiency of TC increases with the increase of biochar dose. When the biochar dose is more than 0.8 g/L, the TC removal rate approaches 100%. This is caused by having more effective sites available for TC adsorption as the biochar dose increases (Zandipak et al., 2019). However, the equilibrium adsorption capacity for TC decreases as the biochar dose increases. For the biochar dose of 0.8 g/L and 1.6 g/L, the adsorption capacity is 24.2 mg/g and 12.2 mg/g, respectively. This phenomenon can be explained that the increasing surface active sites caused by the

increased biochar dose or the decrease in surface active sites due to possible agglomeration of biochar decline the adsorption capacity on average quality of biochar (Zhang et al., 2019b). This results in a reduced adsorption quantity per unit mass of adsorbent. To take this further, the biochar dose is selected as 0.2 g/L in a subsequent experiment. Fig. 2(c) displays the effect of initial TC concentration for TC adsorption. As the concentration varies from 10 to 400 mg/L, TC adsorption capacity increases clearly. This is linked with the increase in the TC concentration difference (biochar surface and the liquid phase) which results in a higher mass transfer rate (Paunovic et al., 2019).

3.2.2 Effect of initial solution pH

It is known that the adsorption performance for adsorbents is affected by the solution pH. This is caused by the alteration of the adsorbent surface charges and the speciation variation of the TC molecules. Here we measure TC adsorption at different initial solution pH values (Fig. 2(d)). Fig. 2(e) shows that TC presents four species including H_4TC^+, H_3TC, H_2TC^- and HTC^{2-} in different pH ranges due to its amphoteric nature (Zhou et al., 2017). From Fig. 2(f), the pH_{PZC} value of HMC-800 is measured to be 3.69. The surface charge of HMC-800 is positive at solution pH values less than its pH_{PZC}, otherwise it is negative. Therefore, at pH 3 and 11, TC molecules (H_4TC^+ and HTC^{2-}) generate repulsive interactions with the surface of HMC-800, yielding a lower adsorption capacity (40.5 and 49.8 mg/g). When the initial pH is varied from 5 to 7, the TC uptake gradually increases with an increase in

pH since TC molecules are normally zwitterions with weak charge. The maximum adsorption value of TC on HMC-800 is observed to be 56.2 mg/g at initial pH 7. An interesting phenomenon found is that TC uptake on HMC-800 was as much as 55.8 mg/g at pH 9, although electrostatic repulsion occurs obviously at this pH. This indicates that there are other interactions between the TC and HMC-800 including hydrogen-bonding, n-π or π-π interactions. From the above statement, the electrostatic attraction/repulsion plays an important but not prevailing role in the TC adsorption process.

Fig. 2

3.2.3 Adsorption kinetics

Adsorption kinetic study is of great importance in evaluating the mechanism of adsorption reactions. Therefore, the kinetics study of TC uptake onto the HMC-800 is here described by a pseudo-first-order, a pseudo-second-order, and an intra-particle diffusion model based on Eqs. (3)-(5).

$$q_t = q_e(1 - e^{-k_1 t}) \tag{3}$$

$$q_t = \frac{k_2 q_e^2 t}{(1 + k_2 q_e t)} \tag{4}$$

$$q_t = k_{ip} t^{1/2} + C \tag{5}$$

In Eqs. (3)-(5), q_e and q_t represent the TC adsorption level (mg/g) at equilibrium and time t (min), respectively. k_1 (min^{-1}), k_2 (g/(mg·min)), and k_{ip} (g/(mg·min)) are the related kinetic constants determined from the pseudo-first-order, pseudo-second-order, and intra-particle diffusion models, respectively. C (mg/g) represents the boundary

layer thickness.

The fitting results of kinetics experiments are summarized in Fig. 3(a) and Table 2. The applied pseudo-second-order model shows a larger non-liner correlation coefficient (R^2 > 0.990). Also, the calculated adsorption value $q_{e,cal}$ (53.4, 87.5, and 115.9 mg/g) offer a better approximation of the experimental values $q_{e,exp}$ (56.2, 86.7, and 118.3 mg/g) compared with that of the pseudo-first-order model $q_{e,cal}$ (51.2, 83.6, and 111.0 mg/g) under different initial TC concentration. It can be inferred that chemisorption was involved between TC molecules and HMC-800, relating to the exchange and interconnection of the electrons between the TC molecules and the surface functional groups of biochar (Zeng et al., 2019). In addition, the pseudo-second-order kinetic constants k_2 is measured to be less than 1, indicating that adsorption process is fast. It can be also noted that k_2 value decreases gradually as the initial TC concentration increases, which could be because of the increasing competitiveness of active sites at higher TC concentrations, resulting in higher adsorption removal rate (Zeng et al., 2019).

The intra-particle diffusion model is analyzed for understanding the diffusion mechanisms and evaluating the main rate-determining step. Three linear curves representing three stages of adsorption, the surface diffusion, intra-particle diffusion, and balance adsorption are shown in Fig. 3(b) (Zbair et al., 2018). When the fitting curves pass through the origin, the rate-determining step for adsorption is associated with the internal diffusion. For our measurements, the curve does not pass through the

origin, suggesting that the intra-particle diffusion is not the only rate-determining step for TC adsorption. In addition, the diffusion constants of these three stages, $k_{ip1} > k_{ip2} > k_{ip3}$, indicate that the external surface diffusion has a more pronounced contribution in the adsorption of TC molecules to the biochar surface. A higher C_2 value illustrates a thicker boundary layer, which demonstrates the main control for TC adsorption on HMC-800 is the intra-particle diffusion (Zeng et al., 2021).

Fig. 3

Table 2

3.2.4 Adsorption isotherm

To further understand the adsorption mechanism of TC on HMC-800, the experimental data collected at different temperatures are fitted using the following models, represented by Eqs. (6)-(10).

The Langmuir equation:

$$q_e = \frac{q_{max} K_L C_e}{1 + K_L C_e} \tag{6}$$

The Freundlich equation:

$$q_e = K_F C_e^{\frac{1}{n}} \tag{7}$$

The Dubinin-Radushkevich equation:

$$q_e = Q_{DR} e^{-K_{DR}\varepsilon^2} \tag{8}$$

$$\varepsilon = RT \ln\left(1 + \frac{1}{C_e}\right) \tag{9}$$

$$E = \frac{1}{\sqrt{2K_{DR}}} \quad (10)$$

where q_e and Q_{DR} (mg/g) represent the TC-adsorbed quantity; C_e (mg/L) represents the TC equilibrium concentration; q_{max} (mg/g) represents the maximum amounts of the adsorbed TC; K_L and K_F are the respective Langmuir and Freundlich constant; n reflects adsorption intensity for TC; K_{DR} (mol^2/J^2) is the D-R constant related to the sorption energy; ε and E (kJ/mol) represent the Polanyi potential and the average adsorption energy.

The three adsorption isotherms have their own assumptions in explaining the adsorption process. Langmuir isotherm assumes that the monolayer adsorption occurs onto the adsorbent surface filling with finite energetically equivalent identical sites (Jang et al., 2018). Freundlich isotherm assumes that the adsorption is carried out on heterogeneous surfaces and more heterogeneity as *1/n* decreases (Hu et al., 2019). The Dubinin-Radushkevich model is widely used to decide whether the adsorption process is physical or chemical using the free energy value *E* (kJ/mol) (Zhou et al., 2017). The parameters of the fitted models at 15, 25 and 35 ℃ are summarized in Fig. 4(a) and Table 3. Based on R^2, a better fit of equilibrium data is observed using Freundlich model ($R^2 > 0.991$). This suggests that the TC uptake on HMC-800 is a heterogeneous process. Meanwhile, $0.1 < 1/n < 1$ demonstrated that the adsorption on HMC-800 is favorable at all temperatures.

The Dubinin-Radushkevich model reflects the physical or chemical properties of adsorption mechanism based on the value of free energy *E* (kJ/mol). It is observed

that the *E* values (0.129, 0.069, and 0.082 kJ/mol at 15, 25 and 35 ℃, respectively), as displayed in Table 3, are lower than 8 kJ/mol, suggesting that physisorption occurred in TC adsorption (Zhou et al., 2017). Therefore, physical and chemical adsorption mechanisms may contribute synergistically towards delivering TC adsorption of HMC-800. A similar conclusion is reported in the literature for g-MoS_2 decorated biochar used for TC removal (Zeng et al., 2018).

Langmuir model provides a good fit for the isotherm data (R^2 > 0.922). This is commonly applied to study the theoretical q_{max} for adsorbents. Here, the adsorption capacities of TC on HMC-800 reaches the maximum values of 138.2, 209.8, and 238.7 mg/g for 15, 25 and 35 ℃, respectively. The q_{max} values of carbonaceous adsorbents reported in the literature were compared and listed in Table S2. The HMC-800 shows an outstanding TC adsorption capacity. Therefore, it is expected that HMC-800 is a promising adsorbent to remove TC.

Fig. 4

Table 3

3.2.5 Thermodynamic study

Reaction temperature plays an important role in adsorption experiments based on several literature studies (Tran et al., 2019; Zhang et al., 2019b). Fig. 4(a) shows that higher temperatures are more favorable for increased adsorption capacity. This manifests that the adsorption process of TC on HMC-800 is endothermic. The pecking order of q_{max} values at different temperatures (from 15 ℃ to 35 ℃) is measured at

138.2 mg/g < 209.8 mg/g < 238.7mg/g. This phenomenon may be explained by the enlarged pores of carbon spheres with rising the temperature. While larger adsorbates molecules can access the enlarged pores, pollutants with smaller molecules (such as phenol) are not favorably adsorbed on such biochar samples (Tran et al., 2019).

We study the thermodynamic properties to further understand the adsorption behavior and its mechanism. Equations (11)-(13) are applied to calculate the standard Gibbs free energy (ΔG^0, kJ/mol), enthalpy (ΔH^0, kJ/mol), and entropy (ΔS^0, $J \cdot mol^{-1} \cdot K^{-1}$).

$$\Delta G^0 = - RT \ln K^0 \quad (11)$$

$$\Delta G^0 = \Delta H^0 - T\Delta S^0 \quad (12)$$

$$\ln K^0 = \frac{\Delta S^0}{R} - \frac{\Delta H^0}{RT} \quad (13)$$

where K^0 refers to the adsorption dispersion coefficient defined by plotting ln (q_e/C_e) against q_e, and the intercept value of lnK^0 is obtained (Yuan et al., 2009); T (K) and R (8.314 J/(mol·K)) represent the reaction temperature and the universal gas constant.

From Table 4, the ΔG^0 values for all temperatures are negative, indicating the TC adsorption on HMC-800 is a spontaneous process. ΔG^0 values decrease gradually with rising reaction temperatures, suggesting that it is favorable to adsorb TC at higher temperatures. The positive ΔH^0 value (33.67 kJ/mol) and the ΔS^0 value (139.6 $J \cdot mol^{-1} \cdot K^{-1}$) imply that TC adsorption on the HMC-800 is of an endothermic nature with an increased randomness of solid-liquid interface.

Table 4

3.2.6 Adsorption mechanism

According to the discussion on the effect of initial solution pH (Sections 3.2.2), the electrostatic attraction/repulsion plays an important but not prevailing role in the adsorption process. Thus, it will not be discussed in our study any further.

For HMC-800, the mesoporous structure forms closely to 80% of its total pore volume. Considering the TC molecular size, having mesopores in abundance facilitates TC adsorption by reducing the steric effect (Tang et al., 2018). Furthermore, as a result of adsorption, the V_{Total} for HMC-800 significantly decreases from 0.249 to 0.173 cm^3/g. This is indicated the significant adsorption of the TC molecules. A typical pore filling adsorption mechanism is explained by having large adsorbate molecules entering the internal pores, clogging the micropore pore. This gives rise to the reduction of the determined micropore surface area and volume (Paunovic et al., 2019). However, as shown in Table 1, HMC-800+TC shows a marked increase in S_{BET}, S_{Micro}, and V_{Micro} when compared to the virgin HMC-800. Since the mesopores volume is dominant on the HMC-800, the screening of TC on the adsorbent surface is significant. More micropores are generated concurrently although the clogging of smaller pore occurred as well, as shown in Fig. 5. This explains the simultaneous decrease of S_{Meso} and increase of S_{Micro} after TC adsorption. Considering this, the pore filling may be predominantly responsible for the adsorption mechanism.

Fig. 5

The FTIR spectrum and Raman spectrum of HMC-800+TC compared to the HMC-800 reveal that π-π interaction participates in the adsorption of TC on HMC-800. On the one hand, the FTIR peak position of graphene C=C bond changes from 1423.9 cm^{-1} to 1403.4 cm^{-1} as a result of adsorption. This is because the conjugated structures of TC molecules can become π-electron acceptors due to the existence of benzene ring and C=C double bonds, and interact intimately with the biochar surface abundant in π-electrons (Ocampo-Perez et al., 2019; Zhang et al., 2019a; Tran et al., 2017). Further, the I_D/I_G value of Raman spectrum has increased for HMC-800+TC. The intensity of two characteristic peaks (D-band and G-band) for HMC-800+TC has an evident change due to the significant charge transformation between TC and the biochar. Thus, this proves the occurrence of π-π interaction (Huang et al., 2020; Tran et al., 2020; Yan et al., 2020).

Considering the abundant oxygen-containing groups of HMC-800 from the XPS analysis, they can firmly link with aromatic contaminants through hydrogen-bonding and n-π interaction. After TC adsorption, the FTIR peaks shift of -OH from 3425.3 to 3434.4 cm^{-1} demonstrated that -OH participated in the adsorption process due to the formation of hydrogen-bonding between -OH (H-donor) on adsorbent surface and H-acceptor (oxygen atoms, nitrogen atoms, or aromatic rings of TC) (Paunovic et al., 2019). The shift of -C=O and -C-O peaks to higher wavenumbers could be explained by n-π interaction. Here, the electron donors from carbonyl oxygen groups combined with the TC aromatic rings can act as electron acceptors (Zhang et al., 2019b). In

short, hydrogen-bonding and n-π interaction contribute as the important interaction mechanisms between HMC-800 and TC due to the high oxygen-containing groups density of HMC-800. Summarily, multiple adsorption mechanisms including physical and chemical interactions participate in the TC adsorption of HMC-800. As stated above, the pore filling, hydrogen-bonding and n-π interaction may mainly contribute to adsorption.

3.2.7 Effect of coexisting anions and adsorption in different water samples

We investigated the impact of having naturally occurring anions such as NO_3^-, SO_4^{2-}, HCO_3^-, and PO_4^{3-} on TC adsorption by HMC-800. From Fig. 4(b), only NO_3^- and SO_4^{2-} have a certain inhibitory effect. This can be explained by considering that NO_3^- and SO_4^{2-} can easily occupy the active sites on the HMC-800 surface, preventing the TC molecules from approaching these sites. In contrast, the coexisting HCO_3^- and PO_4^{3-} anions have no obvious effects on TC adsorption.

Considering the heterogeneity and complexity of contaminated water resources, the presence of various organic or inorganic substrates can influence the adsorption capability of the biochar. Thus, different water samples including water from rivers, lakes, reservoirs, tap water, ground water, as well as deionized water with/without humic acid (5 mg/L), are collected and used to examine the removal efficiency of TC on HMC-800. The influence of different substrates on TC adsorption performance of HMC-800 is shown in Fig. 4(c). The results show that HMC-800 has a larger equilibrium adsorption capacity for TC in the DI water comparing to other real water

matrix. However, regardless of the water matrix used, the adsorption capacity of TC on HMC-800 exceeded 42.3 mg/g, which indicates that HMC-800 has an excellent adsorption performance in practical water matrix and is suitable for environmental remediation.

3.2.8 Regeneration of HMC-800

Renewability is an important factor to evaluate the application feasibility of these adsorbents at large scale. Thus, NaOH (0.1 M), Ethanol (the mass fraction of 95%), and thermal treatment are applied to investigate the reusability of HMC-800. Fig. 4(d) shows that the uptake of TC significantly decreases with the repeated use of the adsorbents when NaOH and ethanol are used in the desorption step. After the fifth usage, the HMC-800 shows a reduction in TC uptake from 56.7 to 8.3 and 2.2 mg/g, respectively. This can be associated with the strong affinity between the TC and HMC-800, resulting in the irreversible utilization of adsorption sites after TC uptake. In contrast, TC uptake is remarkably improved by applying thermal regeneration. Using thermal regeneration, the adsorption capacity of HMC-800 is 98.8, 98.1, 100.0, and 99.0 mg/g after four reuse cycles. This can be explained by the high-temperature activation of 800 ℃ which promotes further development of the biochar channels, and increase of the π-π interaction derived from the increasing π-electrons within HMC-800. We conclude that thermal treatment is effective for the regeneration of HMC-800.

4. Conclusions

We prepare mesoporous batatas biochar using soft-template method and use it for TC removal from water. Our results show that the mesoporous biochar displays a higher specific surface area (286.3 m^2/g) and total pore volume (0.249 cm^3/g) compared to HBC-800 and PBC-800. This indicates that the soft-template agent F127 plays an important role in the formation of pore structures resulting in an improved TC adsorption performance. HMC-800 exhibits a high adsorption capability towards TC, and the maximum adsorption capacity reaches 238.7 mg/g calculated by Langmuir model. In addition, Pseudo-second-order kinetic and Freundlich isotherm models better describe the observed adsorption process. Our thermodynamic studies indicate that the adsorption behavior of TC on HMC-800 is spontaneous, endothermic, resulting in an increased randomness. Here, possible adsorption mechanisms include pore filling, electrostatic force, hydrogen-bonding, n-π or π-π interaction, of which the pore filling, hydrogen-bonding and n-π interaction mechanisms may be prevailing. HMC-800 has a better regeneration performance and adsorption capability in practical water matrix, which suggests that it is a suitable candidate for high-efficiency TC remediation.

Acknowledgment

The Authors thank for financial support from the grant Advanced manufacturing of biochar in UK/China/Malaysia/Nigeria (British Council, UK-China-BRI Countries Education Partnership Initiative, 2019), the China National Natural Science

Foundation (Grant No. 51378205), and the Natural Science Foundation of Henan (Grant No. 182300410136).

References

Ardakani, S., Cheraghi, M., Jafari, A., Zandipak, R., 2020. PECVD synthesis of ZnO/Si thin film as a novel adsorbent for removal of azithromycin from water samples. Int. J. Environ. An. Ch.

Cao, J., Lai, L., Lai, B., Yao, G., Chen, X., Song, L., 2019. Degradation of tetracycline by peroxymonosulfate activated with zero-valent iron: Performance, intermediates, toxicity and mechanism. Chem. Eng. J. 364, 45-56.

Choi, Y.-K., Choi, T.-R., Gurav, R., Bhatia., S.K., Park, Y.-L., Kim, H.J., Kan, E., Yang, Y.-H., 2020. Adsorption behavior of tetracycline onto *Spirulina* sp. (microalgae)-derived biochars produced at different temperatures Sci. Total Environ. 710, 136282.

Delgado-Moreno, L., Bazhari, S., Gasco, G., Méndez, A., El Azzouzi, M., Romero, E., 2021. New insights into the efficient removal of emerging contaminants by biochars and hydrochars derived from olive oil wastes. Sci. Total Environ. 752, 141838.

Fan, S., Wang, Y., Li, Y., Wang, Z., Xie, Z., Tang, J., 2018. Removal of tetracycline from aqueous solution by biochar derived from rice straw. Environ. Sci. Pollut. R. 25(29), 29529-29540.

Feng, S., Li, W., Wang, J., Song, Y., Elzatahry, A.A., Xia, Y., Zhao, D., 2014.

Hydrothermal synthesis of ordered mesoporous carbons from a biomass-derived precursor for electrochemical capacitors. Nanoscale. 6(24), 14657-14661.

Ghoochian, M., Panahi, H., Sobhanardakani, S., Taghavi, L., Hassani, A., 2018. Synthesis and application of Fe_3O_4/SiO_2/thermosensitive/PAMAM-CS nanoparticles as a novel adsorbent for removal of tamoxifen from water samples. Microchem. J. 145, 1231-1240.

Gong, X., Zhao, R., Peng, M., Wang, D., 2019. Experimental study on NO removal by surface activated bamboo charcoal. Atmos. Pollut. Res. 10(2), 474-479.

Hu, X., Jia, L., Cheng, J., Sun, Z., 2019. Magnetic ordered mesoporous carbon materials for adsorption of minocycline from aqueous solution: Preparation, characterization and adsorption mechanism. J. Hazard. Mater. 362, 1-8.

Huang, H., Niu, Z., Shi, R., Tang, J., Lv, L., Wang, J., Fan, Y., 2020. Thermal oxidation activation of hydrochar for tetracycline adsorption: the role of oxygen concentration and temperature. Bioresour. Technol. 306, 123096.

Inagaki, M., Toyoda, M., Soneda, Y., Tsujimura, S., Morishita, T., 2016. Templated mesoporous carbons: Synthesis and applications. Carbon. 107, 448-473.

Jain, A., Balasubramanian, R., Srinivasan, M., 2016. Hydrothermal conversion of biomass waste to activated carbon with high porosity: A review. Chem. Eng. J. 283, 789-805.

Kueasook, R., Rattanachueskul, N., Chanlek, N., Dechtrirat, D., Watcharin, W.,

Amornpitoksuk, P., Chuenchom, L., 2020. Green and facile synthesis of hierarchically porous carbon monoliths via surface self-assembly on sugarcane bagasse scaffold: Influence of mesoporosity on efficiency of dye adsorption. Micropor. Mesopor. Mater. 296, 110005.

Li, J., Wei, L., Jiang, Q., Liu, C., Zhong, L., Wang, X., 2020. Salt-template assisted synthesis of cornstalk derived hierarchical porous carbon with excellent supercapacitance. Ind. Crop. Prod. 154, 112666.

Li, L., Song, H., Chen, X., 2006. Ordered mesoporous carbons from the carbonization of sulfuric-acid-treated silica/triblock copolymer/sucrose composites. Micropor. Mesopor. Mater. 94, 9-14.

Martins, A.C., Pezoti, O., Cazetta, A.L., Bedin, K.C., Yamazaki, D.A.S., Bandoch, G.F.G., Asefa, T., Visentainer, J.V., Almeida, V.C., 2015. Removal of tetracycline by NaOH-activated carbon produced from macadamia nut shells: Kinetic and equilibrium studies. Chem. Eng. J. 260, 291-299.

Meng, Y., Gu, D., Zhang, F., Shi, Y., Cheng, L., Feng, D., Wu, Z., Chen, Z., Wan, Y., Stein, A., 2006. A family of highly ordered mesoporous polymer resin and carbon structures from organic− organic self-assembly. Chem. Mater. 18(18), 4447-4464.

Ocampo-Perez, R., Padilla-Ortega, E., Medellin-Castillo, N.A., Coronado-Oyarvide, P., Aguilar-Madera, C.G., Segovia-Sandoval, S.J., Flores-Ramírez, R., Parra-Marfil, A., 2019. Synthesis of biochar from chili seeds and its application

to remove ibuprofen from water. Equilibrium and 3D modeling. Sci. Total Environ. 655, 1397-1408.

Pachfule, P., Shinde, D., Majumder, M., Xu, Q., 2016. Fabrication of carbon nanorods and graphene nanoribbons from a metal–organic framework. Nat. Chem.

Paunovic, O., Pap, S., Maletic, S., Taggart, M.A., Boskovic, N., Sekulic, M.T., 2019. Ionisable emerging pharmaceutical adsorption onto microwave functionalised biochar derived from novel lignocellulosic waste biomass. J. Colloid Interf. Sci. 547, 350-360.

Pereira, R.C., Arbestain, M.C., Sueiro, M.V., Maciá-Agulló, J., 2015. Assessment of the surface chemistry of wood-derived biochars using wet chemistry, Fourier transform infrared spectroscopy and X-ray photoelectron spectroscopy. Soil Res. 53(7), 753-762.

Sekulic, M.T., Boskovic, N., Slavkovic, A., Garunovic, J., Kolakovic, S., Pap, S., 2019. Surface functionalised adsorbent for emerging pharmaceutical removal: Adsorption performance and mechanisms. Process Saf. Environ. Prot. 125, 50-63.

Sewu, D.D., Jung, H., Kim, S.S., Lee, D.S., Woo, S.H., 2019. Decolorization of cationic and anionic dye-laden wastewater by steam-activated biochar produced at an industrial-scale from spent mushroom substrate. Bioresour. Technol. 277, 77-86.

Shang, Y., Chen, C., Zhang, P., Yue, Q., Li, Y., Gao, B., Xu, X., 2019. Removal of

sulfamethoxazole from water via activation of persulfate by Fe_3C@NCNTs including mechanism of radical and nonradical process. Chem. Eng. J. 375, 122004.

Simsir, H., Eltugral, N., Karagoz, S., 2017. Hydrothermal carbonization for the preparation of hydrochars from glucose, cellulose, chitin, chitosan and wood chips via low-temperature and their characterization. Bioresour. Technol. 246, 82-87.

Sobhanardakani, S., Zandipak, R., 2018. Cerium dioxide nanoparticles decorated on $CuFe_2O_4$ nanofibers as an effective adsorbent for removal of estrogenic contaminants (bisphenol A and 17-α ethinylestradiol) from water. Sep. Sci. Technol. 53(15), 2339-2351.

Tang, L., Yu, J., Pang, Y., Zeng, G., Deng, Y., Wang, J., Ren, X., Ye, S., Peng, B., Feng, H., 2018. Sustainable efficient adsorbent: alkali-acid modified magnetic biochar derived from sewage sludge for aqueous organic contaminant removal. Chem. Eng. J. 336, 160-169.

Tomul, F., Arslan, Y., Kabak, B., Trak, D., Kendüzler, E., Lima, E.C., Tran, H.N., 2020. Peanut shells-derived biochars prepared from different carbonization processes: Comparison of characterization and mechanism of naproxen adsorption in water. Sci. Total Environ. 726, 137828.

Tran, H.N., Tomul, F., Nguyen, H.T.H., Nguyen, D.T., Lima, E.C., Le, G.T., Chang, C.-T., Masindi, V., Woo, S.H., 2020. Innovative spherical biochar for

pharmaceutical removal from water: Insight into adsorption mechanism. J. Hazard. Mater. 394, 122255.

Tran, H.N., Wen, Y.C., Wang, Y.F., You, S.J., 2019. Highly efficient removal of hazardous aromatic pollutants by micro-nano spherical carbons synthesized from different chemical activation methods: a comparison study. Environ. Technol. 40(9-12), 1376-1391.

Tran, H.N., You, S., Chao, H., 2017. Fast and efficient adsorption of methylene green 5 on activated carbon prepared from new chemical activation method. J. Environ. Manage. 188, 322-336.

Turk Sekulic, M., Boskovic, N., Slavkovic, A., Garunovic, J., Kolakovic, S., Pap, S., 2019. Surface functionalised adsorbent for emerging pharmaceutical removal: Adsorption performance and mechanisms. Process Saf. Environ. Prot. 125, 50-63.

Wang, T., Zhang, Z., Zhang, H., Zhong, X., Liu, Y., Liao, S., Yue, X., Zhou, G., 2019. Sorption of carbendazim on activated carbons derived from rape straw and its mechanism. RSC Adv. 9, 41745-41754.

Wu, Q., Gao, M., Zhang, G., Zhang, Y., Liu, S., Xie, C., Yu, H., Liu, Y., Huang, L., Yu, S., 2019. Preparation and application performance study of biomass-based carbon materials with various morphologies by a hydrothermal/soft template method. Nanotechnology. 30(18), 185702.

Wu, Z., Fan, L., Tao, Y., Wang, W., Wu, X., Zhao, J., 2018. Pomelo Peel Derived

Hierarchical Porous Carbon as Electrode Materials for High-Performance Supercapacitor. Chinese J. Inorg. Chem. 34(7), 1249-1260.

Xiao, P., Zhao, L., Sui, Z., Xu, M., Han, B., 2017. Direct synthesis of ordered mesoporous hydrothermal carbon materials via a modified soft-templating method. Micropor. Mesopor. Mater. 253, 215-222.

Xiong, W., Zeng, G., Yang, Z., Zhou, Y., Zhang, C., Cheng, M., Liu, Y., Hu, L., Wan, J., Zhou, C., 2018. Adsorption of tetracycline antibiotics from aqueous solutions on nanocomposite multi-walled carbon nanotube functionalized MIL-53 (Fe) as new adsorbent. Sci. Total Environ. 627, 235-244.

Xu, Q., Han, B., Wang, H., Wang, Q., Zhang, W., 2020. Effect of extracellular polymer substances on the tetracycline removal during coagulation process. Bioresour. Technol. 309, 123316.

Yan, L., Liu, Y., Zhang, Y., Liu, S., Wang, C., Chen, W., Liu, C., Chen, Z., Zhang, Y., 2020. ZnCl2 modified biochar derived from aerobic granular sludge for developed microporosity and enhanced adsorption to tetracycline. Bioresour. Technol. 297, 122381.

Yu, B., Bai, Y., Ming, Z., Yang, H., Chen, L., Hu, X., Feng, S., Yang, S., 2017. Adsorption behaviors of tetracycline on magnetic graphene oxide sponge. Mater. Chem. Phys. 198, 283-290.

Yu, D., Yi, X., Ma, Y., Yin, B., Zhuo, H., Li, J., Huang, Y., 2009. Effects of administration mode of antibiotics on antibiotic resistance of Enterococcus

faecalis in aquatic ecosystems. Chemosphere. 76(7), 915-920.

Yuan, X., Xing, W., Zhuo, S., Han, Z., Wang, G., Gao, X., Yan, Z., 2009. Preparation and application of mesoporous Fe/carbon composites as a drug carrier. Micropor. Mespor. Mat. 117(3), 678-684.

Zandipak, R., Sobhanardakani, S., 2018. Novel mesoporous $Fe_3O_4/SiO_2/CTAB\text{-}SiO_2$ as an effective adsorbent for the removal of amoxicillin and tetracycline from water. Clean Technol Envir. 20, 871-885.

Zandipak, R., Sobhanardakani, S., Shirzadi, A., 2019. Synthesis and application of nanocomposite $Fe_3O_4@SiO_2@CTAB\text{-}SiO_2$ as a novel adsorbent for removal of cyclophosphamide from water samples. Sep. Sci. Technol. 53(3), 456-470.

Zbair, M., Ahsaine, H.A., Anfar, Z., 2018. Porous carbon by microwave assisted pyrolysis: An effective and low-cost adsorbent for sulfamethoxazole adsorption and optimization using response surface methodology. J. Clean. Prod. 202(20), 571-581.

Zeng, S., Choi, Y.-K., Kan, E., 2021. Iron-activated bermudagrass-derived biochar for adsorption of aqueous sulfamethoxazole: Effects of iron impregnation ratio on biochar properties, adsorption, and regeneration. Sci. Total Environ. 750, 141691.

Zeng, Z., Ye, S., Wu, H., Xiao, R., Jie, G., 2019. Research on the sustainable efficacy of g-MoS_2 decorated biochar nanocomposites for removing tetracycline hydrochloride from antibiotic-polluted aqueous solution. Sci. Total Environ.

648, 206-217.

Zhang, M., Xu, L., Qi, C., Zhang, M., 2019a. Highly Effective Removal of Tetracycline from Water by Hierarchical Porous Carbon: Batch and Column Adsorption. Ind. Eng. Chem. Res. 58(43), 20036-20046.

Zhang, P., Li, Y., Cao, Y., Han, L., 2019b. Characteristics of tetracycline adsorption by cow manure biochar prepared at different pyrolysis temperatures. Bioresour. Technol. 285, 121348.

Zhang, X., Li, Y., Wu, M., Pang, Y., Hao, Z., Hu, M., Qiu, R., Chen, Z., 2020. Enhanced adsorption of tetracycline by an iron and manganese oxides loaded biochar: kinetics, mechanism and column adsorption. Bioresour. Technol. 320, 124264.

Zhao, Z., Nie, T., Zhou, W., 2019. Enhanced biochar stabilities and adsorption properties for tetracycline by synthesizing silica-composited biochar. Environ. Pollut. 254, 113015.

Zhou, J., Ma, F., Guo, H., 2020. Adsorption behavior of tetracycline from aqueous solution on ferroferric oxide nanoparticles assisted powdered activated carbon. Chem. Eng. J. 384, 123290.

Zhou, Y., He, Y., He, Y., Liu, X., Xu, B., Yu, J., Dai, C., Huang, A., Pang, Y., Luo, L., 2019. Analyses of tetracycline adsorption on alkali-acid modified magnetic biochar: site energy distribution consideration. Sci. Total Environ. 650, 2260-2266.

Zhou, Y., Liu, X., Xiang, Y., Wang, P., Zhang, J., Zhang, F., Wei, J., Luo, L., Lei, M.,

Tang, L., 2017. Modification of biochar derived from sawdust and its application in removal of tetracycline and copper from aqueous solution: Adsorption mechanism and modelling. Bioresour. Technol. 245, 266-273.

Figure Captions

Fig.1. Effect of pyrolytic temperature of sludge biochar (a) and biochar D-BC200 dose (b) on Mo(VI) uptake.

Fig.2. Non-linear (a), linear pseudo-first-order (b) and linear pseudo-second-order (c) simulation for the adsorption of Mo(VI).

Fig.3. Langmuir and Freundlich isotherms for the adsorption of Mo(VI) onto D-BC200 at 288, 298 and 308 K.

Fig.4. Plots of $\ln q_e/C_e$ versus q_e for Mo(VI) adsorption on D-BC200 (a); changes of free energy (thermodynamic calculations) (b).

Fig.5. SEM image (a) and Zeta potential (b) of the biochar D-BC200.

Fig.6. XPS full scans spectra (a), O1s (b) wide scan C1s (c) of the D-BC200 and BC600, C1s of D-BC200 (d) and C1s of BC600 (e).

Fig.7. Effect of coexisting anions (a) and NOM (b) on Mo(VI) uptake.

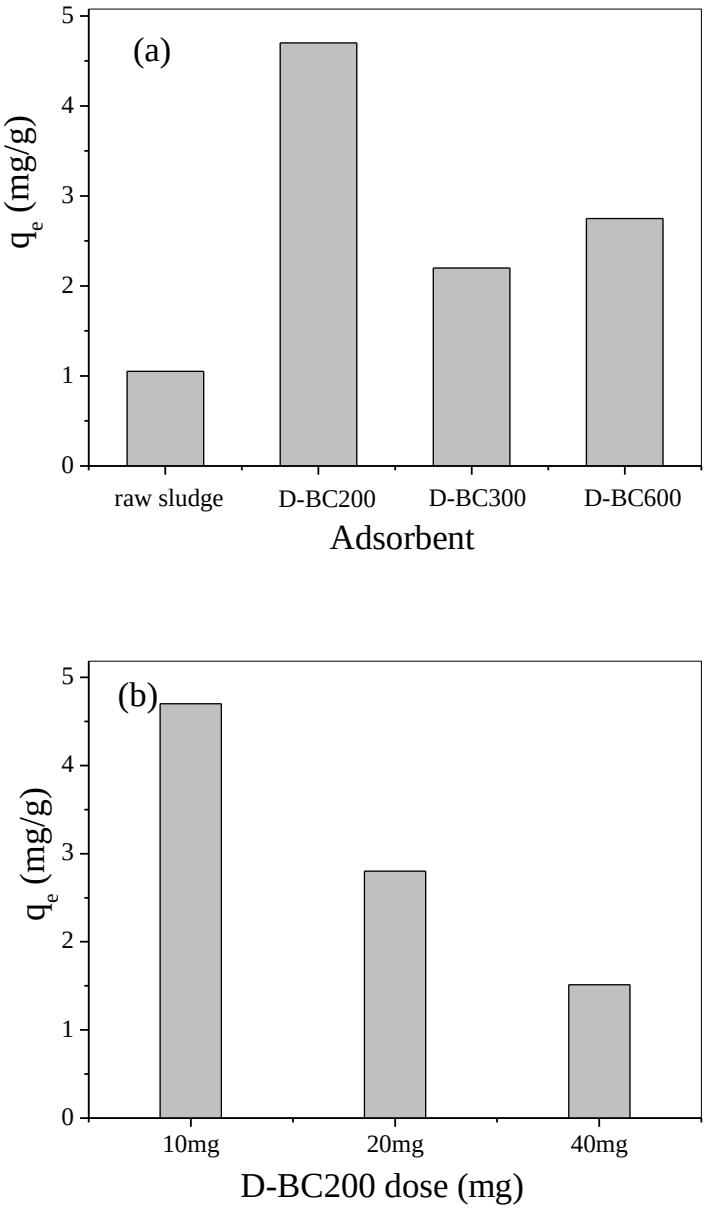
(a)
q_e (mg/g)
0
1
2
3
4
5
raw sludge
D-BC200
D-BC300
D-BC600
Adsorbent
(b)
q_e (mg/g)
0
1
2
3
4
5
10mg
20mg
40mg
D-BC200 dose (mg)

Fig.1

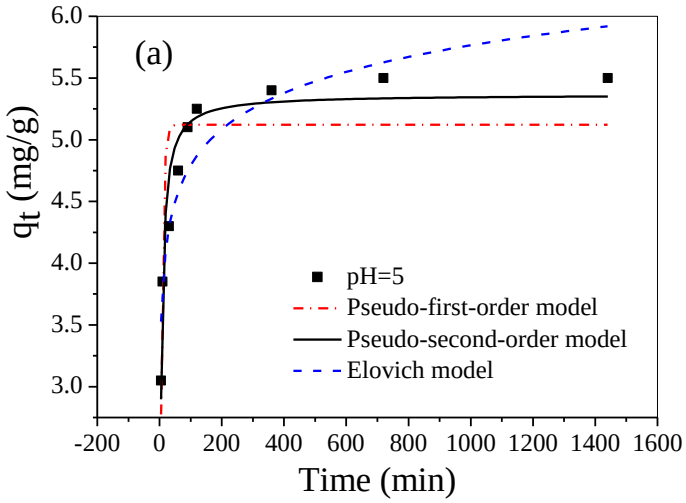
(a)
q_t (mg/g)
Time (min)
pH=5
Pseudo-first-order model
Pseudo-second-order model
Elovich model

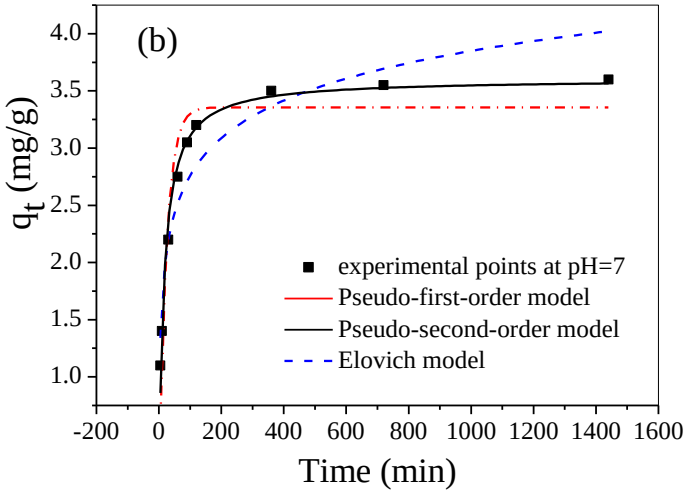
(b)
q_t (mg/g)
Time (min)
experimental points at pH=7
Pseudo-first-order model
Pseudo-second-order model
Elovich model

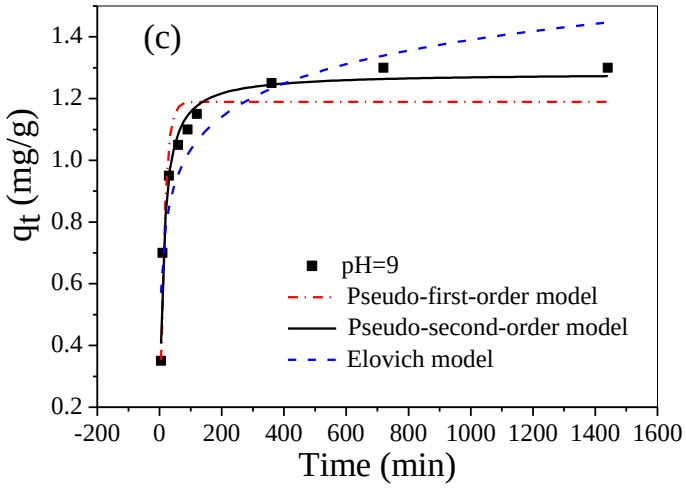
(c)
q_t (mg/g)
Time (min)
pH=9
Pseudo-first-order model
Pseudo-second-order model
Elovich model

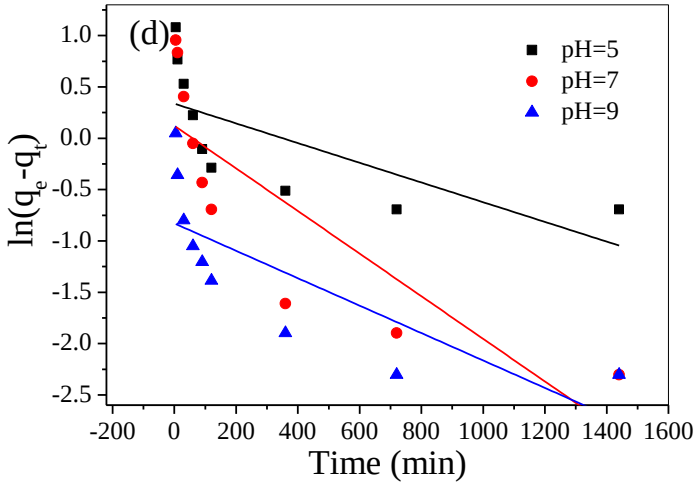

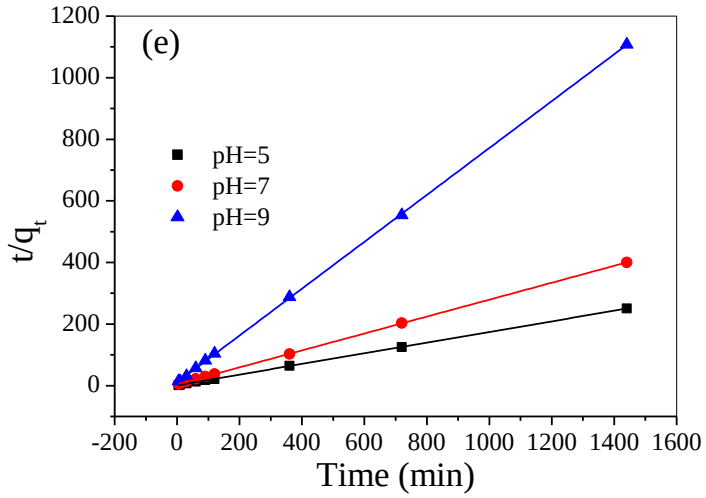

Fig.2

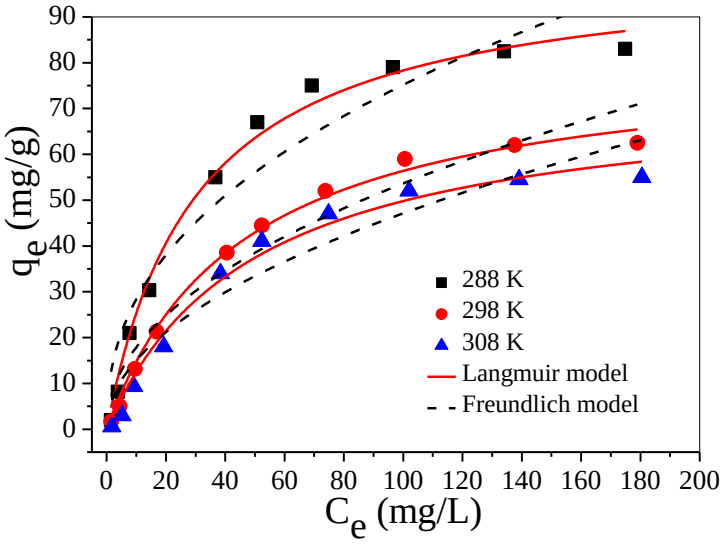
90
80
70
60
50
40
30
20
10
0
q_e (mg/g)
0
20
40
60
80
100
120
140
160
180
200
C_e (mg/L)
288 K
298 K
308 K
Langmuir model
Freundlich model

Fig.3

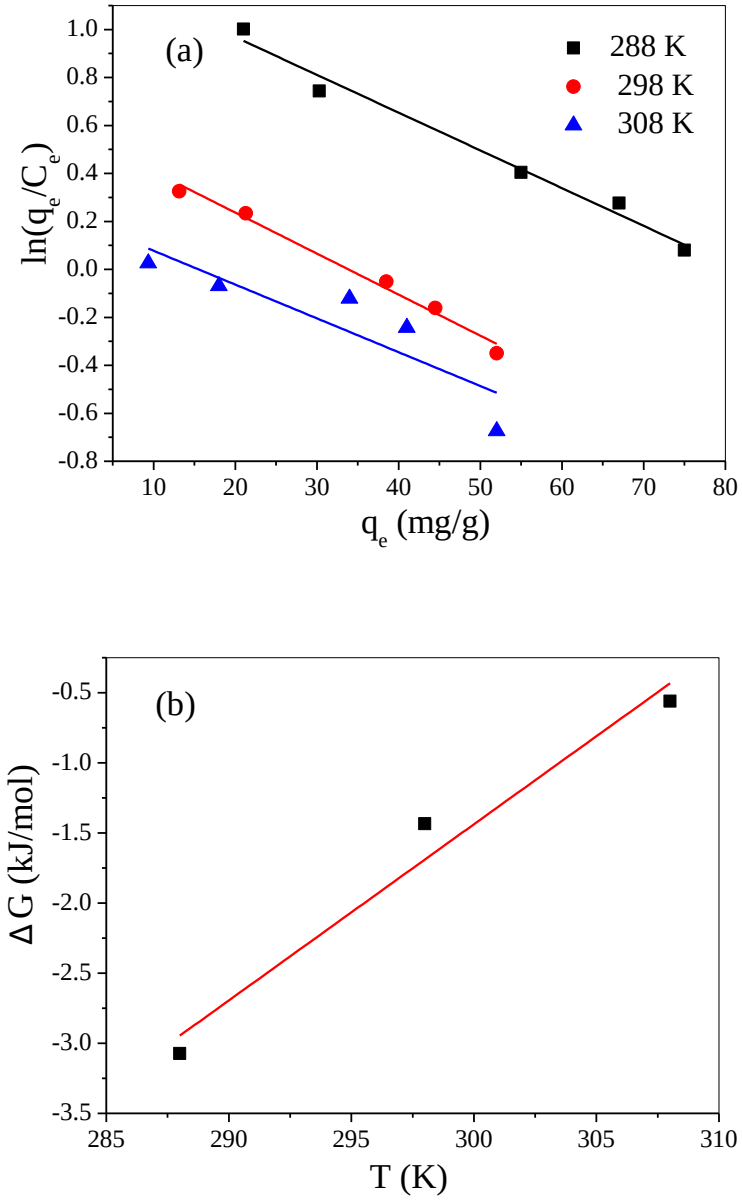
(a)
288 K
298 K
308 K
ln(q_e/C_e)
q_e (mg/g)
1.0
0.8
0.6
0.4
0.2
0.0
-0.2
-0.4
-0.6
-0.8
10
20
30
40
50
60
70
80
(b)
ΔG (kJ/mol)
T (K)
-0.5
-1.0
-1.5
-2.0
-2.5
-3.0
-3.5
285
290
295
300
305
310

Fig.4

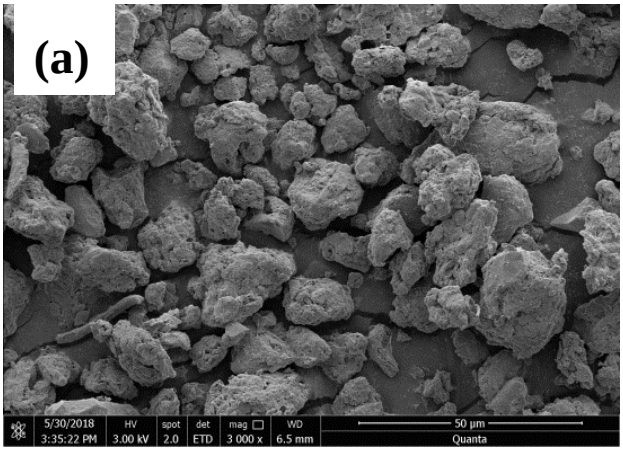
(a)
5/30/2018
3:35:22 PM
HV
3.00 kV
spot
2.0
det
ETD
mag
3 000 x
WD
6.5 mm
50 µm
Quanta

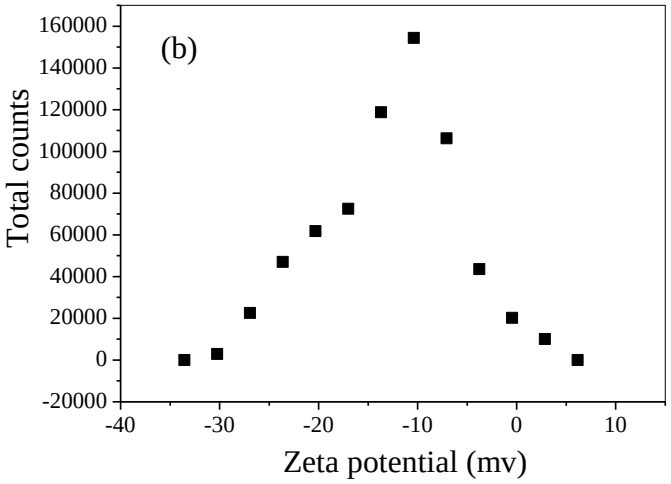
(b)
Total counts
160000
140000
120000
100000
80000
60000
40000
20000
0
-20000
-40
-30
-20
-10
0
10
Zeta potential (mv)

Fig.5

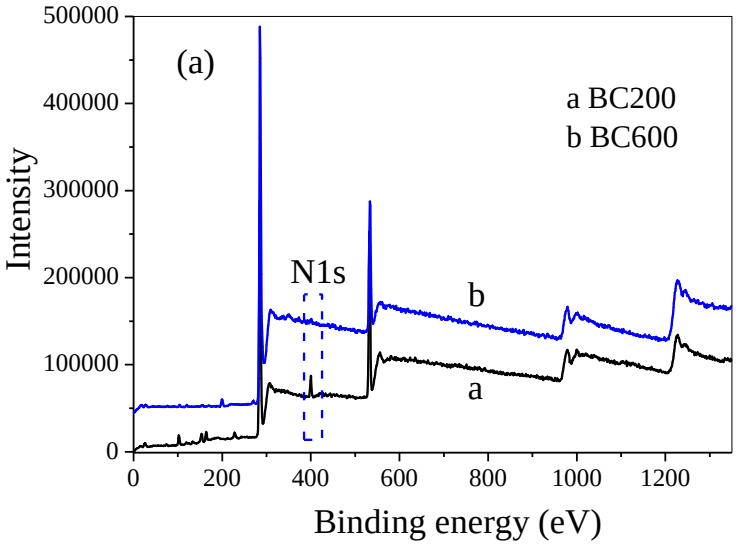
(a)
a BC200
b BC600
N1s
b
a
Intensity
Binding energy (eV)
500000
400000
300000
200000
100000
0
0
200
400
600
800
1000
1200

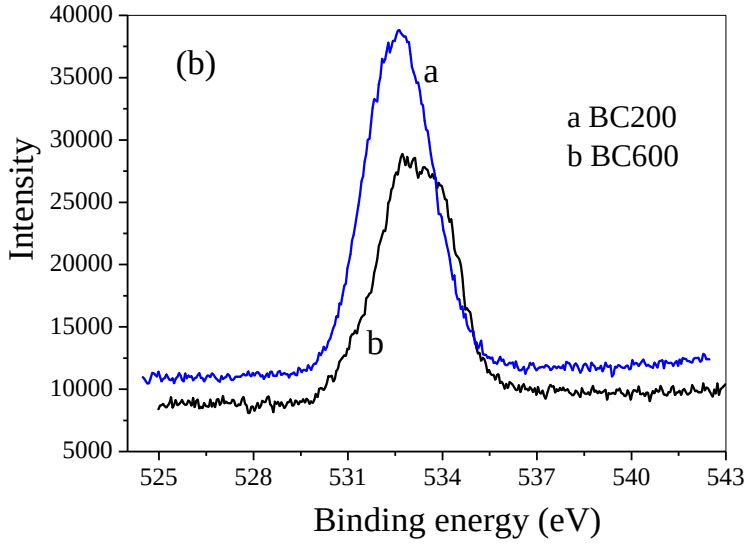
(b)
a
b
a BC200
b BC600
Intensity
Binding energy (eV)
40000
35000
30000
25000
20000
15000
10000
5000
525
528
531
534
537
540
543

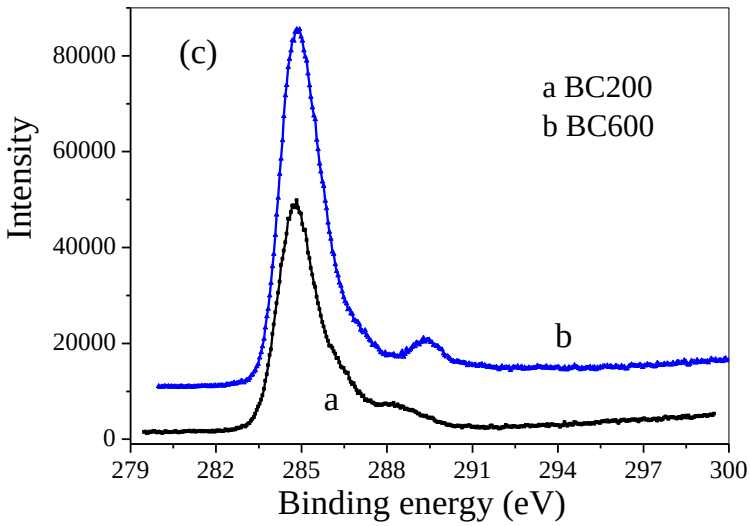
(c)
a BC200
b BC600
b
a
Intensity
Binding energy (eV)
80000
60000
40000
20000
0
279
282
285
288
291
294
297
300

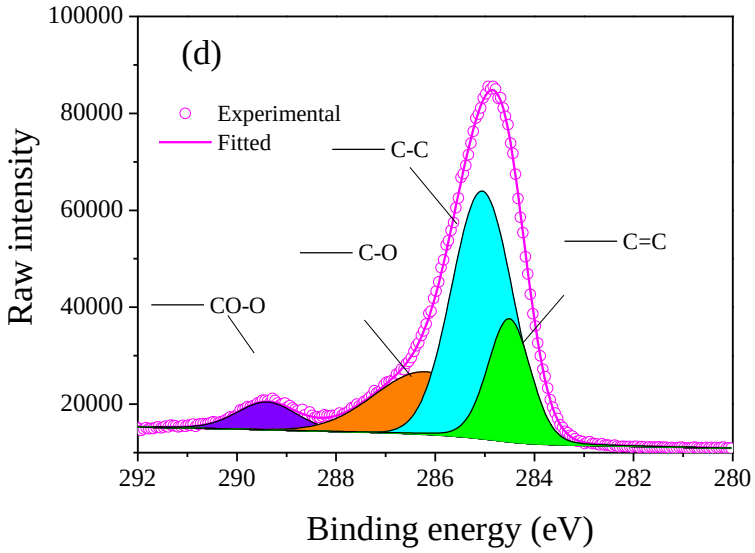
(d)
Experimental
Fitted
C-C
C-O
C=C
CO-O
Raw intensity
Binding energy (eV)
100000
80000
60000
40000
20000
292
290
288
286
284
282
280

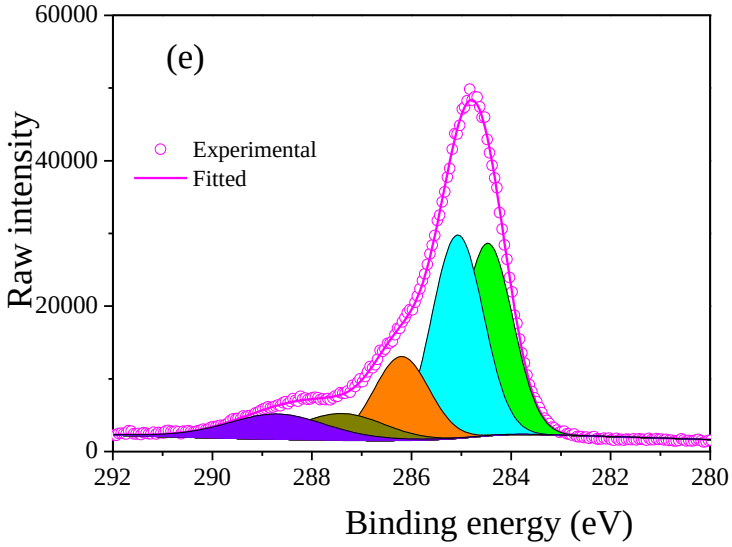
(e)
Experimental
Fitted
Raw intensity
Binding energy (eV)
60000
40000
20000
0
292
290
288
286
284
282
280

Fig.6

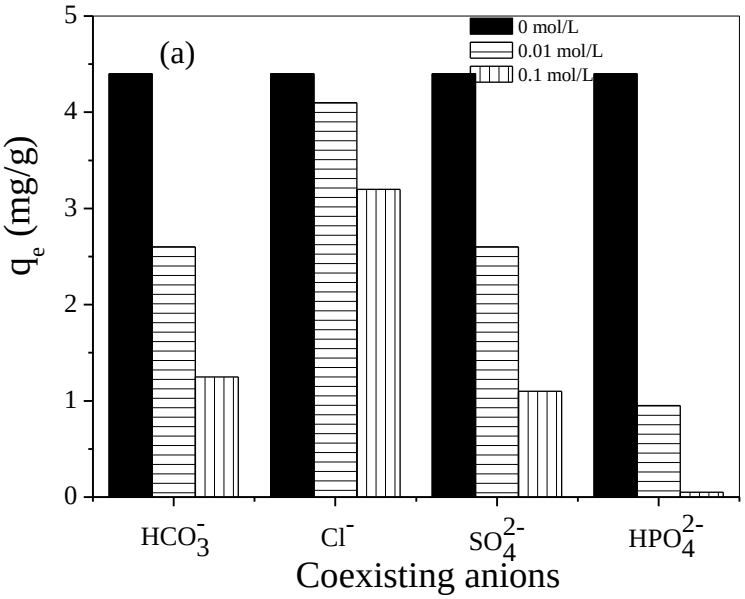
(a)
0 mol/L
0.01 mol/L
0.1 mol/L
q_e (mg/g)
0
1
2
3
4
5
HCO_3^-
Cl^-
SO_4^{2-}
HPO_4^{2-}
Coexisting anions

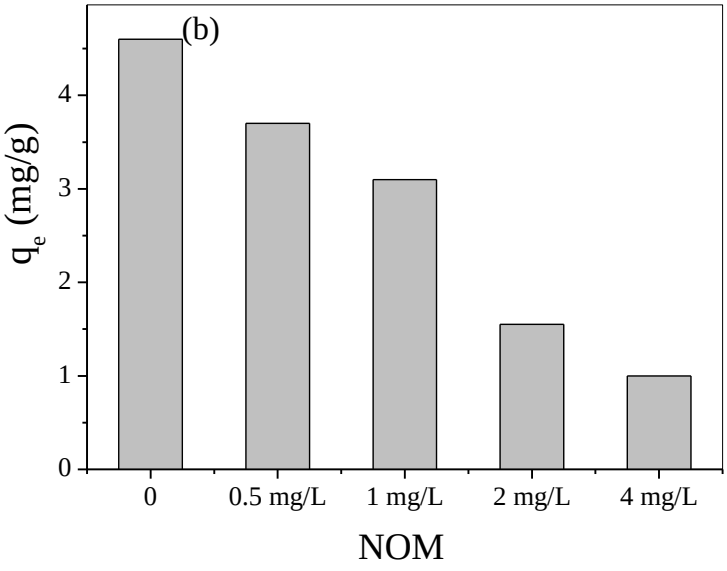
(b)
q_e (mg/g)
0
1
2
3
4
0
0.5 mg/L
1 mg/L
2 mg/L
4 mg/L
NOM

Fig.7

Table 1 Non-linear kinetics parameters simulated by the pseudo-first-order, pseudo-second-order and Elovich models for Mo(VI) adsorption on D-BC200.

model	parameters	pH=5	pH=7	pH=9
	q_e(mg/g)	5.12	3.36	1.19
Pseudo-first-order	k_1(min^{-1})	0.156	0.041	0.071
	R^2	0.758	0.900	0.897
Pseudo-second-order	q_e(mg/g)	5.37	3.61	1.28
	k_2(g/(mg min))	0.044	0.017	0.072
	R^2	0.937	0. 985	0.976
Elovich	a	2.847	0.579	0.322
	k	0.422	0.473	0.155
	R^2	0.858	0.896	0.846

Table 2 Linear kinetics parameters simulated by the pseudo-first-order and pseudo-second-order models for Mo(VI) adsorption on D-BC200.

	Pseudo-first-order model			**Pseudo-second-order model**		
	q_e (mg/g)	k_1 (min^{-1})	R^2	q_e (mg/g)	k_2 (mg·g^{-1}·min^{-1})	R^2
pH=5	1.40	0.001	0.432	5.79	0.020	0.999
pH=7	1.13	0.002	0.660	3.64	0.017	0.999
pH=9	0.44	0.001	0.560	1.31	0.055	0.999

Table 3 Langmuir and Freundlich isotherm parameters for the adsorption of Mo(VI) onto D-BC200.

Model	Parameters	288 K	298 K	308 K
Langmuir	q_{max} *(mg/g)*	101.9	82.1	74.3
	k_L (L/mg)	0.033	0.022	0.020
	R^2	0.992	0.995	0.983
Freundlich	K_F ($mg^{(1-1/n)}L^{1/n}/g$)	10.69	5.94	4.80
	n	2.36	2.09	2.02
	R^2	0.916	0.940	0.915

Table 4 Comparison of Mo(VI) adsorption capacities on various sorbents.

Sorbents	q_m (mg/g)	Solution pH	References
sludge biochar D-BC200	82.1	7	This study
WB200	33.4	N.A.	[10]
WB1000	84.0	N.A.	[10]
maghemite	33.4	5	[27]
nano-magnetic $CuFe_2O_4$	30.6	2.8	[9]
mesoporous zirconium silicate	22.8	N.A.	[28]
NaOCl-oxidized multiwalled carbon nanotubes	20.16	neutral	[13]
$ZnCl_2$ activated coir pith carbon	14.4	N.A.	[29]
waste Fe(III)/Cr(III) hydroxide	12.3	Initial pH 4.0	[30]
iron-based adsorbents	10.4	3 mol/L HNO_3	[31]
chitosan adsorbent	124.3	7.8	[12]
Mo(VI) ion-imprinted polymer	126.06	3	[32]

microcrystalline modified with 8-hydroxyquinoline	anthracene	45.1	N.A.	[33]

N.A. = Not available

[b]The suffix of BC indicates the pyrolytic temperature for biochar

Table 5 Thermodynamic parameters at different reaction temperatures.

T (K)	lnk_0	ΔG^0 (kJ·mol^{-1})	ΔH^0(kJ·mol^{-1})	$\triangle S^0$ (J·mol^{-1}·K^{-1})
288	1.28	-3.07	-39.1	-125.6
298	0.58	-1.44	-39.1	-125.6
308	0.22	-0.56	-39.1	-125.6

Table 6 Chemical state assignments for D-BC200 and D-BC600 (%).

	C=C	C-C	C-O	C=O	CO-O
D-BC200	34.3	58.3	3.85	／	3.54
BC600	27.0	26.2	17.7	14.5	14.6